

AIAA 81-0640R

Analysis and Flight Data for a Drone Aircraft with Active Flutter Suppression

Jerry R. Newsom*

NASA Langley Research Center, Hampton, Virginia
and

Anthony S. Pototzky†

Kentron International, Hampton, Virginia

This paper presents a comparison of analysis and flight test data for a drone aircraft equipped with an active flutter suppression system. Emphasis is placed on the comparison of modal dampings and frequencies as a function of Mach number. Results are presented for both symmetric and antisymmetric motion with flutter suppression off. Only symmetric results are presented for flutter suppression on. The analysis correlation is improved by using an empirical aerodynamic correction factor which is proportional to the ratio of experimental to analytical steady-state lift curve slope. The analysis overpredicts the flutter speed with the flutter suppression system off by 4% and overpredicts it by 2% with the system on. In addition to presenting the mathematical models and a brief description of existing analytical techniques, an alternative analytical technique for obtaining closed-loop results is presented.

Nomenclature

$C_{L\alpha}$	= lift curve slope
c	= reference chord
D	= parameter scheduler
$D(s)$	= denominator polynomial
G	= shear modulus
G_a	= antisymmetric filter
G_c	= common filter
G_s	= symmetric filter
g	= acceleration due to gravity
$G(i\omega)$	= vehicle frequency response
$H(i\omega)$	= control law and actuator frequency response
i	$= \sqrt{-1}$
k	= reduced frequency
M	= Mach number
$N(s)$	= numerator polynomial
s	= Laplace variable
t	= time
V	= freestream velocity
w_g	= gust velocity
$Y(s)$	= transfer function input
\ddot{Z}	= vertical acceleration
β	= aerodynamic lag
δ	= control surface motion
δ_c	= actuator command
ζ	= damping ratio
$\ddot{\Theta}_x$	= roll angular acceleration
ρ	= freestream density
ω	= circular frequency

Matrices

$[A]$	= dynamics matrix
$[A_i]$	= real aerodynamic coefficient matrix
$[B]$	= control distribution matrix
$[C]$	= state coefficient output matrix
$[D]$	= input coefficient output matrix
$[D_s]$	= structural damping matrix

$[K]$	= generalized stiffness matrix
$[M]$	= generalized mass matrix
$[Q]$	= generalized aerodynamic force matrix
$\{q\}$	= generalized coordinate vector
$\{u\}$	= input vector
$\{X\}$	= state vector
$\{Y\}$	= output vector

Subscripts

c	= control system
FUS	= fuselage
LW	= left wing
m	= motion
N	= nominal
RW	= right wing
v	= vehicle
w_g	= vertical gust
δ	= control surface
$(\dot{})$	= derivatives with respect to time

Introduction

WITH active control technology, supercritical airfoils, and new materials evolving into viable approaches for reducing aircraft mass, confidence in accurately predicting the dynamic behavior of flexible aircraft incorporating these advancements is important. Because of the potentially destructive nature of flutter, the credibility of modern flutter prediction techniques are of increasing concern to the designer. To gain confidence in the analytical tools and techniques employed, comparisons of analytical results with those obtained from experiment are necessary.

Past NASA research efforts have been directed toward both developing analysis tools and correlating wind-tunnel test results with analytical predictions. Wind-tunnel tests in the transonic region are traditionally limited by model size, dynamic pressure (for aeroelastic tests), and the effects of the interaction between the model and reflected shock waves. As a complement to wind-tunnel tests, flight tests are being conducted in a NASA program called drones for aerodynamic and structural testing (DAST).¹ In this program, unmanned, remote-controlled drone aircraft are used as test beds for high-risk research such as flutter tests. Some of the objectives of this flight program are to explore the accuracy and limitations of flutter predictions for a supercritical wing in the transonic region and to evaluate flutter suppression system (FSS) performance.

Presented as Paper 81-0640 at the AIAA/ASME/ASCE/AHS 22nd Structures, Structural Dynamics and Materials Conference, Atlanta, Ga., April 6-8, 1981; submitted May 26, 1981; revision received Jan. 18, 1982. This paper is declared a work of the U.S. Government and therefore is in the public domain.

*Aerospace Engineer, Loads and Aeroelasticity Division. Member AIAA.

†Senior Engineer, Hampton Technical Center. Member AIAA.

Reference 2 presents results of one of the first wind-tunnel tests of a flexible supercritical wing. The agreement between the measured flutter boundary and the calculated boundary was very good except in the critical transonic region. References 3-5 present results of studies of active control of wing/store flutter for a fighter configuration. Some of the comparisons of analysis and experiment given show reasonably good agreement. Reference 6 presents results for an active flutter margin augmentation system for a commercial transport with a conventional wing. Comparisons between analysis and flight data are given in terms of transfer functions and damping/frequencies and show good agreement. Wind-tunnel tests of a cantilever aeroelastic wing model of the present drone wing with an active FSS are reported in Ref. 7. However, in contrast to the drone aircraft wing section reported here, the wind-tunnel model did not have a supercritical shape. This study showed good agreement for flutter mode frequencies for both the FSS-off and FSS-on cases. Neither damping nor frequency response comparisons were made since these quantities were not experimentally measured. In summary, no flutter tests, either wind-tunnel or flight, of a supercritical wing configuration with active flutter suppression have been reported previously.

This paper is one of three companion papers that describe various aspects of the first few flights in the DAST program. Edwards⁸ presents details of the flutter test technique development and the implementation of the FSS on the vehicle. Bennett and Abel⁹ present the experimental frequency and damping estimates obtained using a postflight parameter estimation technique. This paper is presented as an effort to correlate the results obtained by various analytical techniques with the experimental results given in Ref. 9. The study ranges from the comparison of open-loop frequency responses to the comparison of flexible mode damping/frequency differences for both symmetric and antisymmetric motion. In addition, a description of the analytical techniques and mathematical models used in the study is given.

Description of Drone Aircraft

The geometry of the drone aircraft is shown in Fig. 1. The wing has an aspect ratio of 6.8 with a supercritical airfoil designed for cruise at $M=0.98$. The small outboard control surfaces on each wing have the dual function of both suppressing flutter through the control system and providing excitation for measurement purposes. Accelerometers located on the rear spar near the wing tip are used to sense motion for the FSS. Fuselage accelerometers are used to subtract the rigid body motion.

Bending stiffness of the wing is provided primarily by two steel spars located at 25 and 60% of the local wing chord. Torsional stiffness is provided primarily by fiberglass skins which are attached to the spars to form the wing box. The fibers in the skin are oriented parallel and normal to the wing elastic axis to create a torsional stiffness which is low enough to allow flutter to occur within the flight envelope. In addition, a ballast is added to the outboard section aft of the trailing edge to further reduce the flutter speed.

The drone has been modified to improve controllability and acquisition of research data. Flight tests involve air launches from beneath the wing of a B-52 and midair recovery by a helicopter. A description of the operational procedures is given in Refs. 1 and 8.

Analytical Techniques and Mathematical Models

Equations of Motion

The equations of motion are formulated through the conventional modal approach. The motion of the vehicle is described by a linear combination of its free vibration modes. The forcing functions to the system are both control and gust

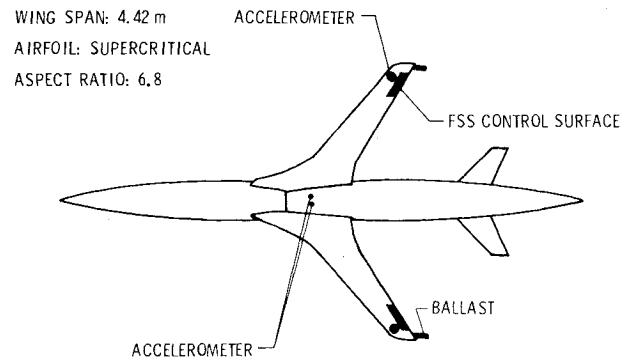


Fig. 1 Vehicle geometry.

inputs. Therefore, the basic equations of motion can be written as

$$[M]\{\ddot{q}\} + [D_s]\{\dot{q}\} + [K]\{q\} + \frac{1}{2}\rho V^2 [Q_m(t)]\{q\} = -\frac{1}{2}\rho V^2 [Q_\delta(t)]\{Q_{w_g}(t)\} \left\{ \frac{\delta}{w_g/V} \right\} \quad (1)$$

All of the coefficients in these equations, with the exception of the aerodynamic terms, are independent of time. The aerodynamic force matrices are complex valued and normally represented as tabular functions of reduced frequency, $k=c\omega/2V$. To obtain a set of constant coefficient differential equations, the unsteady aerodynamic force matrices are approximated by a rational polynomial in the Laplace variable s

$$[Q(s)] = [A_0] + [A_1] \left(\frac{cs}{2V} \right) + [A_2] \left(\frac{cs}{2V} \right)^2 + \sum_{j=1}^4 \frac{[A_{2+j}]s}{s + (2V/c)\beta_j} \quad (2)$$

After selecting a set of aerodynamic lags β_j , the coefficient matrices $[A_i]$ are computed by a least squares curve fit in a fashion similar to that described in Ref. 10.

By equating derivatives to the powers of the Laplace operator s , the equations of motion for the basic vehicle can be written in standard state-space form as follows:

$$\begin{aligned} \dot{X}_v &= [A_v]\{X_v\} + [B_v]\{u_v\} \\ Y_v &= [C_v]\{X_v\} + [D_v]\{u_v\} \end{aligned} \quad (3)$$

where

$$\{X_v\} = \begin{Bmatrix} q \\ \dot{q} \\ X_{\beta_1} \\ \vdots \\ \dot{X}_{\beta_4} \end{Bmatrix}, \{u_v\} = \begin{Bmatrix} \delta \\ \dot{\delta} \\ \ddot{\delta} \\ w_g \\ \dot{w}_g \\ \ddot{w}_g \end{Bmatrix}, \{Y_v\} = \text{sensor outputs}$$

The matrix $[A_v]$ is a $6n \times 6n$ matrix where n is the number of modes.

Stability Analysis

A brief description of the analytical methods used to calculate stability with both FSS-off and FSS-on will be presented in this section. In particular, an alternate method

for the FSS-on calculations which differs from that given in Ref. 10 is presented.

FSS-Off

The matrix $[A_v]$ in Eq. (3) is a function of Mach number, velocity, and density. For fixed values of Mach number, velocity, and density, the eigenvalues of $[A_v]$ are the roots of the FSS-off flutter equation. Variation of the roots of the flutter equation as a function of altitude at constant Mach number can be computed. This approach yields a "match point" solution without the necessity of cross-plotting several density calculations as with the conventional V - g flutter solution. The flutter boundary for the basic vehicle is determined by performing the calculations at several Mach numbers.

FSS-On

An alternate approach from that of Ref. 10 is employed to formulate the FSS-on equations. To use this approach, both the actuator and control law models are written in standard state-space form and then interconnected to the basic vehicle equations. This approach is used because it requires the solution of a much smaller order eigenvalue problem than the approach described in Ref. 10.

A single control input and single sensor output will be used to illustrate this technique, but the same technique can be extended to multiple controls and sensors. The control law and actuator dynamics are normally represented by transfer functions which can be combined and written in the form

$$\delta(s)/Y(s) = N(s)/D(s) \quad (4)$$

where

$N(s)$ = numerator polynomial, in s

$D(s)$ = denominator polynomial, in s

There are many ways of expressing this transfer function in state-space form. The technique used in this paper is described in Ref. 11. The development uses a Frobenius form realization to obtain the matrix coefficients. As shown in Ref. 11, the system defined by the transfer function of Eq. (4) can be written in state-space form as

$$\begin{aligned} \{\dot{X}_c\} &= [A_c]\{X_c\} + [B_c]Y_c \\ \{u_c\} &= [C_c]\{X_c\} \end{aligned} \quad (5)$$

where

Y_c = transfer function input

$$\{u_c\} = \begin{Bmatrix} \delta \\ \dot{\delta} \\ \ddot{\delta} \end{Bmatrix}$$

The matrix $[A_c]$ is an $nc \times nc$ matrix where nc is the order of $D(s)$ in Eq. (4). It is important to note that when using this approach the control displacement and its first and second derivatives must be made available as inputs to the basic vehicle system. This implies that the transfer function needs to be at least third order to obtain the higher derivatives and avoid any direct transfer term from Y_c .

The interconnection of systems is most often described by the "state augmentation technique."¹² In the present application, consider the systems described by Eqs. (3) and (5). Defining the augmented state as

$$\{X\} = \begin{Bmatrix} X_v \\ X_c \end{Bmatrix} \quad (6)$$

and using the relations that $\{u_v\} = \{u_c\}$ and $Y_c = Y_v$, the closed-loop or FSS-on dynamics are represented by

$$\begin{aligned} \{\dot{X}\} &= \begin{bmatrix} A_v & B_v C_c \\ B_c C_v & A_c \end{bmatrix} \{X\} \\ \{\dot{X}\} &= [A]\{X\} \end{aligned} \quad (7)$$

where $[A]$ is a $(6n + nc) \times (6n + nc)$ matrix. As in the FSS-off equations, the matrix $[A]$ in Eq. (7) is a function of Mach number, velocity, and density. For fixed values of Mach number, velocity, and density the eigenvalues of $[A]$ are the roots of the FSS-on flutter equation. Variations in Mach number and/or density can be used to predict modal dampings and frequencies and the FSS-on flutter boundary.

Structural Model

The structural model is a NASTRAN[†] finite-element model of the wing, wing center section, fuselage, and empennage. The wing model was originally developed by Teledyne Ryan Aeronautical and then updated to a complete vehicle model by both Boeing-Wichita¹³ and NASA Langley. A drawing of the updated NASTRAN model is presented in Fig. 2a.

The wing finite-element idealization includes the leading- and trailing-edge structures which are modeled with elements providing stiffness for translational degrees of freedom only. The spars and ribs are modeled with rods and shear elements. The fiberglass wing skins are modeled using shear elements with rods added to represent the membrane stiffness. The wing center section is modeled with beam and plate elements lying in a horizontal plane. The wing is connected to the wing center section with single-point connections at the front and rear spars.

Elastic axis representations employing beam elements are used in modeling the fuselage, vertical tail, and horizontal stabilizer. The connections between the wing center section and the fuselage are defined by constraint equations relating translations at the side of body to the motions of the elastic axis at the fuselage centerline. To simplify the structural representation, appropriate centerline constraints are used to define separately both symmetric and antisymmetric motion.

Ten symmetric and ten antisymmetric elastic modes were computed and used for analysis purposes. The symmetric modes cover a frequency range of 9.1-105.0 Hz, the antisymmetric modes a frequency range of 12.3-80.7 Hz. A ground vibration test was performed on the vehicle to measure both symmetric and antisymmetric modes and frequencies. A comparison between the measured and analytical frequencies is presented in Table 1. For both the symmetric and antisymmetric cases, the frequency of mode 1 (primarily first-wing bending) is underpredicted and the frequency of mode 3 (primarily first-wing torsion) is overpredicted.

Unsteady Aerodynamic Model

The unsteady aerodynamic matrices in Eq. (1) are calculated using the doublet-lattice program in the ISAC system.¹⁴ The frequency-dependent unsteady aerodynamic pressure distributions are calculated by subdividing each lifting surface into an array of streamwise trapezoidal boxes. The wing and empennage sections are aerodynamically modeled as shown in Fig. 2b. The model includes 121 boxes for the wing, 14 boxes for the horizontal tail, and 8 boxes for the vertical tail. The aerodynamic effect of the fuselage is assumed to be negligible. Eight boxes are used to model the wing control surface shown by the shaded area. The unsteady aerodynamic forces are calculated for 2 rigid body modes, 10

[†]NASTRAN is a registered trademark of the National Aeronautics and Space Administration.

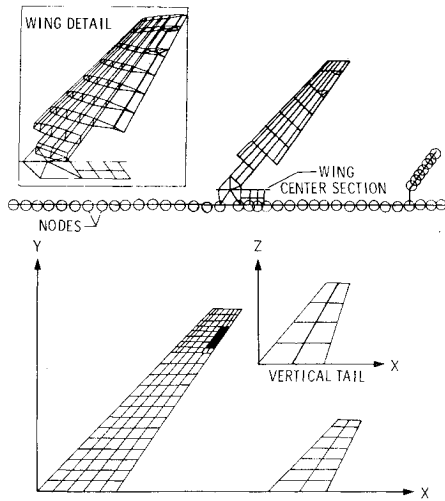


Fig. 2 Structural and aerodynamic models.

Table 1 Analysis and GVT^a vibration frequencies

Mode	Symmetric		Antisymmetric	
	Analysis	GVT	Analysis	GVT
1	9.1	9.6	12.3	13.5
2	16.5	16.2	21.7	19.3
3	29.6	29.1	30.0	27.0
4	34.0	31.2	34.2	31.0
5	39.8	40.6	36.0	—
6	48.6	48.5	48.3	48.4
7	65.2	—	53.7	—
8	71.1	—	54.0	—
9	78.9	—	77.4	—
10	105.0	—	80.7	—

^aGVT = ground vibration test.

elastic modes, a control surface rotation, and a sinusoidal gust.

The aerodynamic lag terms β_j used in approximating the unsteady aerodynamics in the s plane are somewhat arbitrary, but are usually chosen to lie somewhere within the range of interest of the reduced frequencies. Choosing the β_j terms spaced evenly in the reduced-frequency range of interest usually provides a good approximation. The reduced-frequency range of interest for this application is 0.0-0.4. The selected values are 0.1, 0.2, 0.3, and 0.4.

Actuator Model

The control surface is driven by a rotary actuator located at the inboard edge of the control surface. The actuator is controlled by a servovalve mounted in the wing center section. The servoactuators use actuator shaft position and differential load pressure feedback. Displacement and rate requirements for the control surface were determined during the flutter suppression system design and performance evaluation and are discussed in Ref. 15. The actuator was sized to provide a control surface displacement of ± 12 deg and rate of 920 deg/s.

The original analytical model of the actuator, described in Ref. 15, was derived by Boeing-Wichita. The model predicted an actuator bandwidth near 100 Hz. However, when the system was assembled and bench tested, the bandwidth was approximately 70 Hz. The bench test indicated a hydraulic fluid mode near 110 Hz. This fluid mode is not accounted for in the analytical model. The presence of this mode contributed to the reduction in bandwidth. Furthermore, when the actuator was installed in the flexible wing, the final bandwidth reduced to approximately 55 Hz. At this point a significant effort was expended to increase the bandwidth and resulted in the implementation of several notch filters to stabilize high-frequency (100-400 Hz) hydraulic modes.

Because of these complications, the original actuator model was not used in the analysis. Instead, the actuator model is

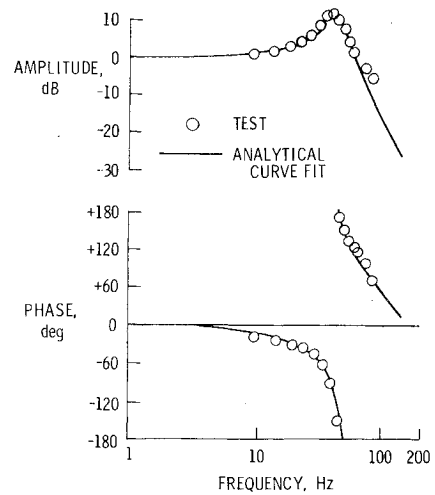


Fig. 3 Bode plot of actuator dynamics.

derived from a measured frequency response to a 1 deg amplitude sinusoid input with the actuator installed in the wing. The measured frequency response data was curve fit with a sixth-order transfer function. This resulted in the following transfer function:

$$\delta(s)/\delta_c(s) = 2.7 \times 10^{16} / [(s^2 + 76.8s + 8.7 \times 10^4) \times (s^2 + 589.4s + 1.9 \times 10^5) (s^2 + 502.7s + 1.6 \times 10^6)], \text{deg/deg} \quad (8)$$

Figure 3 presents a Bode plot showing the comparison between the frequency response using Eq. (8) and the measured data. It is interesting that later studies indicate little change in the response characteristics with the inclusion of airloads. However, a substantial decrease in bandwidth and corresponding increase in phase lag was observed when the response was measured for an 8 deg input amplitude.

FSS Control Law

The FSS was designed by Boeing-Wichita under contract to NASA-Langley. A description of the design of the control law is given in Ref. 15. However, between the second and third flights described in Ref. 8, Boeing-Wichita performed a redesign of the control law. A block diagram of the redesigned FSS is presented in Fig. 4. The redesigned control law is used in all analyses presented in this paper. The initial summation of sensors provides left- and right-wing vertical accelerations minus the rigid body accelerations due to vertical and roll accelerations. These signals are fed into the common filters G_c and then summed to form the symmetric filtered signal and differenced to form the antisymmetric filtered signal. These signals are filtered by the symmetric G_s and antisymmetric G_a filters, then summed and differenced, and multiplied by a gain of 0.5 to form the left and right control surface commands. The transfer functions for the common, symmetric, and antisymmetric filters are given by

$$\begin{aligned} G_c &= \frac{2.25 \times 10^6 s (s^2 + 76s + 295^2) (s^2 + 120s + 306^2)}{(s+2) (s+295)^2 (s^2 + 240s + 324^2) (s+1500)^2} \\ &\times \frac{(s^2 + 60s + 1037^2) (s^2 + 76s + 1269^2)}{(s^2 + 300s + 1037^2) (s^2 + 500s + 1269^2)} \\ G_s &= \frac{-1.6 (s^2 + 100s + 71^2) (s^2 + 100s + 168^2)}{(s^2 + 100s + 58^2) (s^2 + 100s + 112^2)} \\ G_a &= \frac{-2.528 (s^2 + 100s + 158^2)}{(s^2 + 80s + D)} \end{aligned} \quad (9)$$

where $D = 49,000 - 804 \times (\frac{1}{2} \rho V^2)$.

Experimental Data and Discussion of Results

Experimental Data Acquisition

The control surfaces are used both for suppressing flutter and for exciting the wing responses. A fast swept sine wave, which varies at 10.0-40.0 Hz in 8 s, is used for exciting the wing. The two control surfaces are oscillated either in phase or out of phase for symmetric or antisymmetric motion, respectively. Measurements in the form of time histories of the responses, command signals, and control surface positions are made and relayed to ground facilities for recording. Frequency response functions of the flexible vehicle are obtained from the time histories through the use of fast Fourier transform (FFT) techniques. Both the modal characteristics and the frequency response functions are obtained from the data presented in Ref. 9.

Comparison of Analysis with Flight Test Results

It is well known that linear, thin-wing, potential flow theory starts to lose its validity when approaching the transonic region and is therefore not able to give satisfactory approximations to the aerodynamic forces. There are several empirical methods used to improve the representation of the aerodynamic forces in this region. Probably the most common method uses experimental steady-state aerodynamic force data. Using a relatively straightforward approach, a correction factor based on the steady-state lift curve slope ($C_{L\alpha}$) is applied to all unsteady aerodynamic force data. Specifically, this correction factor is obtained by calculating, at each Mach number, the ratio of experimental-to-analytical $C_{L\alpha}$ for the vehicle. Figure 5a presents a comparison of the experimental-to-analytical $C_{L\alpha}$ for the drone aircraft (experimental values are taken from Ref. 16). The lift curve slope is underpredicted throughout the Mach number range. The ratio of experimental to analytical $C_{L\alpha}$ varies from 1.03 ($M=0.70$) to 1.18 ($M=0.95$). This correction factor is then applied to the generalized aerodynamic force matrix by multiplying all elements by this factor, which has an effect equivalent to increasing density. Figure 5b demonstrates the

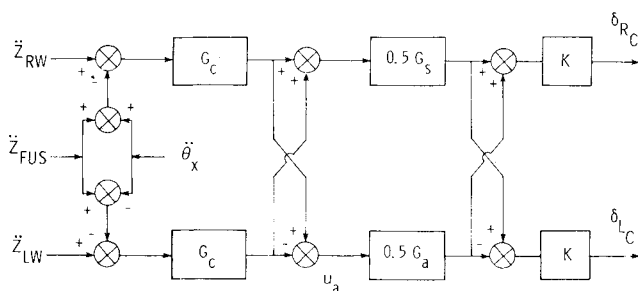


Fig. 4 Block diagram of the flutter suppression system.

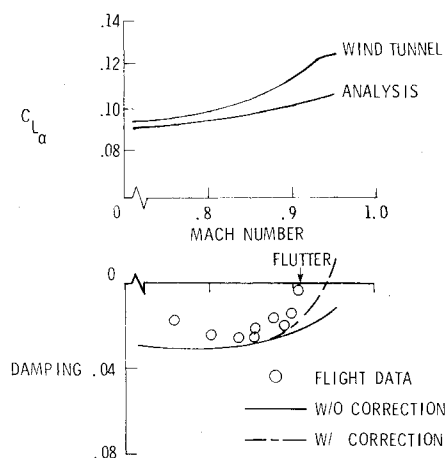


Fig. 5 Effect of aerodynamic correction factor.

use of the correction factor in the flutter analysis. The flutter Mach number is shifted more toward the flight test point resulting in a better agreement. Consequently, the correction factor will be used in all analytical results presented.

The predicted flutter boundary and the flight test points for the FSS-off case are presented in Fig. 6 for both symmetric and antisymmetric motions. The difference between the flight test and prediction at constant altitude is approximately 0.02-0.03 in Mach number. There could be many reasons for this difference, but a plausible explanation that was examined was the nonlinear behavior of the stiffness properties of the fiberglass skins. More precisely, the shear modulus for the fiberglass skin was experimentally determined to vary substantially (nearly 50%) with shear stress as shown in Fig. 7. Since shear stress increases and therefore the shear modulus decreases as Mach number (dynamic pressure) increases, this effect could be important in flutter predictions. Therefore, flutter calculations (only for the symmetric case) were performed for a shear modulus variation of $\pm 20\%$ from the nominal value ($G_N = 0.58 \times 10^{10}$). The results of these calculations are also presented in Fig. 6. These parameter variations more than adequately bracket the data points obtained from the flight tests.

Frequency and damping characteristics were obtained from two flight tests. The symmetric and antisymmetric results shown in Figs. 8 and 9, respectively, were obtained from the first flight test at an altitude of 7.62 km. The change in frequency of the bending (mode 1) and torsion (mode 2)

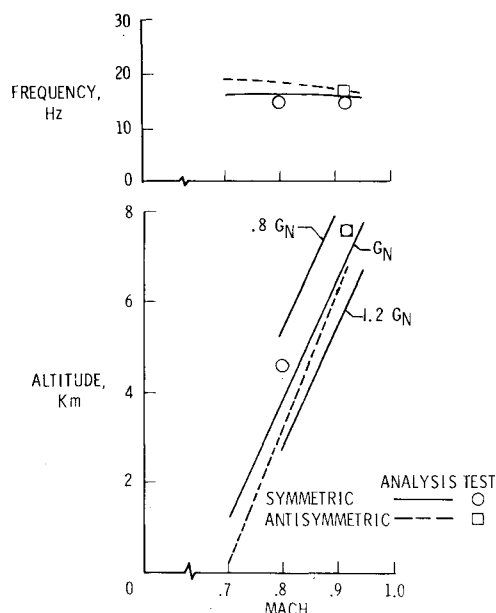


Fig. 6 Flutter boundary (FSS-off).

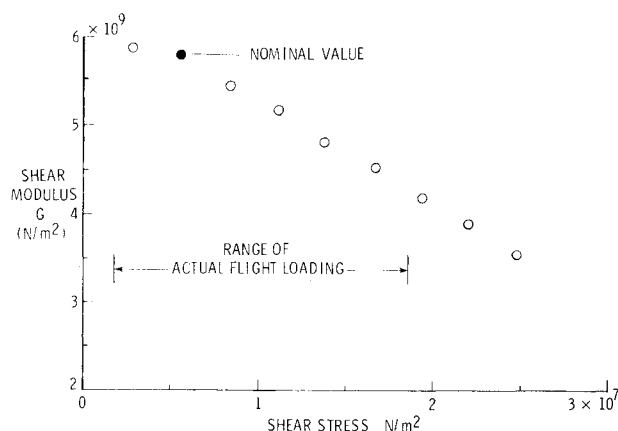


Fig. 7 Shear modulus variation with shear stress.

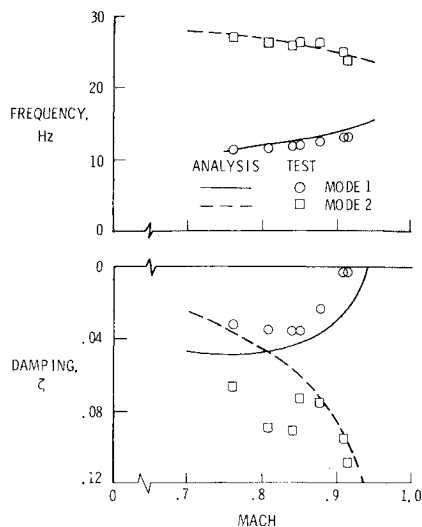


Fig. 8 Damping and frequency variations with Mach number at 7.62 km (symmetric, FSS-off).

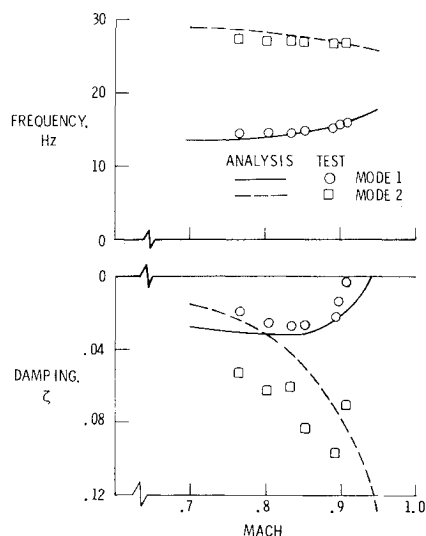


Fig. 9 Damping and frequency variations with Mach number at 7.62 km (antisymmetric, FSS-off).

modes with Mach number were well predicted for both symmetric and antisymmetric motions. However, the damping over the same range of Mach numbers was overpredicted by analysis for the flutter mode (mode 1) and underpredicted for the torsion mode (mode 2). From previous works^{3,6} where damping was experimentally and analytically available, the analysis usually overpredicted the damping of the flutter mode. This is consistent with the results presented here. These differences require further investigation and this discrepancy should be considered during any FSS design.

The frequency and damping of the dominant mode are presented for both the symmetric and antisymmetric cases in Figs. 10 and 11, respectively. The analysis and experiment correspond to the second flight test at an altitude of 4.57 km. FSS-on results are presented only for the symmetric case. The change in frequency with Mach number is predicted well for both the FSS-off and FSS-on cases. However, analysis overpredicts the damping for both the FSS-off and FSS-on cases as in the 7.62 km results. The experimental flutter speed is extrapolated to be approximately $M=0.80$ for the FSS-off symmetric case (Fig. 10). An actual flutter point was encountered for the FSS-on case at $M=0.82$. The analysis overpredicts the FSS-off flutter speed by 4% and overpredicts the FSS-on flutter speed by 2%.

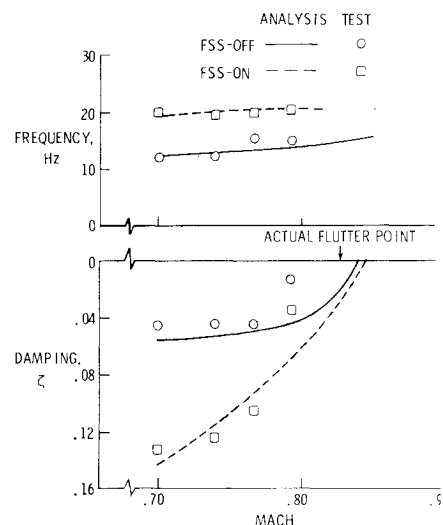


Fig. 10 Damping and frequency variations with Mach number at 4.57 km (symmetric).

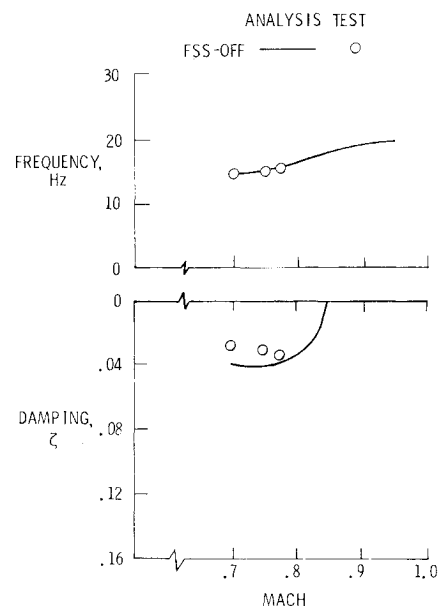


Fig. 11 Damping and frequency variations with Mach number at 4.57 km (antisymmetric).

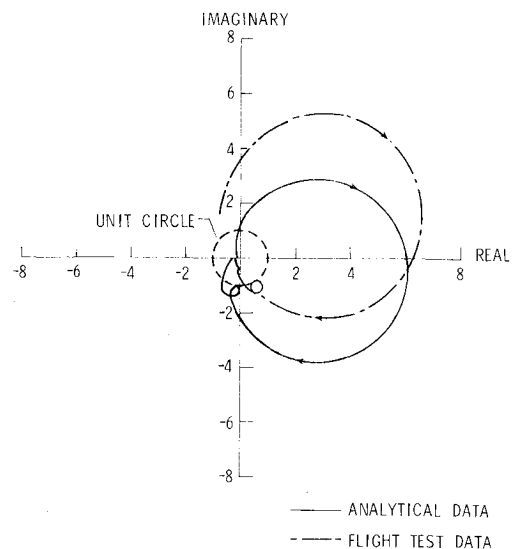


Fig. 12 Nyquist diagram of open-loop system at $M=0.70$ and 4.57 km (symmetric).

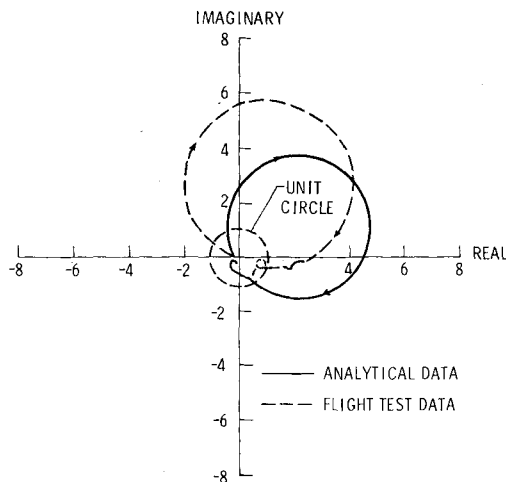


Fig. 13 Nyquist diagram of open-loop system at $M=0.70$ and 4.57 km (antisymmetric).

An alternate method based on frequency response techniques was used to compare flight data to analysis. The frequency domain responses of the vehicle were obtained by FFT techniques from the time responses recorded during flight tests. To compare directly with the analysis open-loop frequency response $[G(i\omega) \times H(i\omega)]$, the experimentally obtained frequency response $[G(i\omega)]$ was augmented by the control law and actuator dynamics $[H(i\omega)]$. The results at $M=0.70$ and 4.57 km are plotted in the form of Nyquist diagrams in Figs. 12 and 13. Some smoothing was necessary to reduce the observed scatter apparent in the transformed FFT raw flight data. The lobes represent elastic resonance points in the vehicle dynamics and the fact that the lobes in the analysis do not coincide angularly with the ones from the flight data illustrate the phase differences between the two results. There appears to be a better agreement in frequencies for the symmetrical case than the antisymmetrical case when comparing selected frequency points of the two results.

Conclusion

A comparison of analysis and flight test data for a drone aircraft equipped with active flutter suppression has been presented. Although absolute values of the test results were not predicted, the analysis did predict the trends reasonably well. In particular, modal frequencies were predicted with good success. However, flutter mode damping was in most instances overpredicted. The flutter speed was overpredicted by 3-4% for the FSS-off case and overpredicted by 2% for the FSS-on case. This nonconservatism is believed to be a result of the nonlinear torsional stiffness associated with the shear modulus of the fiberglass skin and the aerodynamics of the

supercritical airfoil. These results suggest more care is needed in modeling structures in terms of nonlinear properties and understanding the aerodynamic mechanisms which contribute to the differences between analysis and test.

References

- ¹Murrow, H.N. and Eckstrom, C.V., "Drones for Aerodynamic and Structural Testing (DAST)—A Status Report," *Journal of Aircraft*, Vol. 16, Aug. 1979, pp. 521-526.
- ²Farmer, M.G., Hanson, P.W., and Wynne, E.C., "Comparison of Supercritical and Conventional Wing Flutter Characteristics," NASA TM X-72837, 1976.
- ³Gravelle, A., "Active Flutter Control in Transonic Conditions," Paper presented at the Symposium IUTAM Structural Control, Waterloo, Belgium, June 4-7, 1979.
- ⁴Hwang, C., Winther, B.A., Mills, G.P., Noll, T.E., and Farmer, M.G., "Demonstration of Aircraft Wing/Store Flutter Suppression Systems," *Journal of Aircraft*, Vol. 16, Aug. 1979, pp. 557-563.
- ⁵Noll, T.E. and Huttzell, L.J., "Wing Store Active Flutter Suppression—Correlation of Analyses and Wind-Tunnel Data," *Journal of Aircraft*, Vol. 16, July 1979, pp. 491-497.
- ⁶O'Connell, R.F. and Messina, A.F., "Development of an Active Flutter Margin Augmentation System for a Commercial Transport," *Journal of Guidance and Control*, Vol. 3, Sept.-Oct. 1980, pp. 352-360.
- ⁷Newsom, J.R., Abel, I., and Dunn, H.J., "Application of Two Design Methods for Active Flutter Suppression and Wind-Tunnel Test Results," NASA TP-1653, 1980.
- ⁸Edwards, J.W., "Flight Test Results of an Active Flutter Suppression System Installed on a Remotely Piloted Research Vehicle," AIAA Paper 81-0655, April 1981.
- ⁹Bennett, R.M. and Abel, I., "Application of a Flight Test and Data Analysis Technique to Flutter of a Drone Aircraft," AIAA Paper 81-0652, April 1981.
- ¹⁰Abel, I., "An Analytical Technique for Predicting the Characteristics of a Flexible Wing Equipped with an Active Flutter Suppression System and Comparison with Wind-Tunnel Data," NASA TP-1367, Feb. 1979.
- ¹¹Konar, A.F., Stone, C.R., Mahesh, J.K., and Hank, M., "Active Control Synthesis for Flexible Vehicles. Volume 1—KONPACT Theoretical Description," AFFDL TR-75-146, June 1976 (available from DDC as AD-B0151981).
- ¹²Kwakernaak, H. and Sivan, R., *Linear Optimal Control Systems*, John Wiley & Sons, New York, 1972.
- ¹³Visor, O.E. and Severt, F.D., "Preliminary Design Study of a Flutter Suppression Control System for BQM-34E/F Drone Aircraft with a Supercritical Wing—Final Report," NASA CR-145208, 1976.
- ¹⁴Peele, E.L. and Adams, W.M., Jr., "A Digital Program for Calculating the Interaction Between Flexible Structures, Unsteady Aerodynamics, and Active Controls," NASA TM-80040, 1979.
- ¹⁵McGehee, C.R. and Hodges, G.E., "Final Design and Fabrication of an Active Control System for Flutter Suppression on a Supercritical Aeroelastic Research Wing," NASA CR-165714, June 1981.
- ¹⁶Byrdson, T.A. and Hallissy, J.B., "Longitudinal and Lateral Static Stability and Control Characteristics of a 1/6-Scale Model of a Remotely Piloted Research Vehicle with a Supercritical Wing," NASA TP-1360, 1979.